# Electronic sputtering of solid N_2 by swift ions

E. Dartois, M. Chabot, T. Id Barkach, H. Rothard, P. Boduch, B. Augé, J. Duprat, J. Rojas

# Electronic sputtering of solid $N_2$ by swift ions

E. Dartois[a], M. Chabot[b], T. Id Barkach[b], H. Rothard[c], P. Boduch[c], B. Augé[d], J. Duprat[b], J. Rojas[b]

[a]*Institut des Sciences Moléculaires d'Orsay, UMR8214, CNRS, Université Paris-Saclay, 91405 Orsay, France*
[b]*Laboratoire de physique des deux infinis Irène Joliot-Curie, CNRS-IN2P3, Université Paris-Saclay, 91405 Orsay, France*
[c]*Centre de Recherche sur les Ions, les Matériaux et la Photonique, CIMAP-CIRIL-GANIL, Normandie Université, ENSICAEN, UNICAEN, CEA, CNRS, F-14000 Caen, France*
[d]*Institut de planétologie et d'astrophysique de Grenoble, CNRS, Université Grenoble Alpes, 38000 Grenoble, France*

**Abstract**

Most sputtering yield measurements for solid $N_2$ are reported for stopping powers lower than $10^{-13}$ eV cm$^2$/molecule. We measured the sputtering yield for solid $N_2$ at stopping powers, in the electronic regime, above $10^{-12}$ eV cm$^2$/molecule, extending the range of such measurements by more than an order of magnitude, using a 33 MeV $^{58}Ni^{9+}$ swift heavy ions beam. The evolution of the thin $N_2$ ice films was monitored in-situ by mid-infrared spectroscopy (FTIR) during irradiation. As $N_2$ is only weakly infrared active, and can be hardly monitored directly via an infrared absorption mode in such experiments, we use the Fabry-Perot interference fringes of the ice film to evaluate, via an optical model, the erosion of the $N_2$ film as a function of ion fluence. A sputtering model including several sputtering crater shapes is developed and tested against experimental data. We derive the sputtering yield for a semi-infinite $N_2$ ice film and its dependence with the ice thickness for thin film conditions, monitoring the $N_2$ ice sputtering depth. We combine the results with previous measurements at lower stopping powers to derive the electronic sputtering of solid $N_2$ over a large stopping power range.

*Keywords:* `Electronic sputtering, Radiation chemistry, Heavy ions, Solid N2, Sputtering crater`

## 1. Introduction

The impact of fast ions on insulators such as, in the present case, frozen gases, results in an ionisation track. The high energy primary ion and its induced secondary electrons create repulsive electronic excited states on timescale much shorter than that of changes in the ice structures. A very large part of this energy is converted to the motion of nuclei, and in a time scale of the order of tenths to tens of nanoseconds, a small hot volume appears, often referred as "thermal spike" [1, 2]. This thermal spike thermalises and, near the surface, sudden sublimation occurs. Many laboratory studies have been performed on ice sputtering, in particular in the 80' and 90' using projectiles with low stopping power. Since a decade, large facilities open the possibility to

*Corresponding author.
*Email address:* `emmanuel.dartois@universite-paris-saclay.fr` (E. Dartois)

access to projectiles with high stopping power. Such studies provide realistic numbers to determine the effects of heavy cosmic rays (CR) in the dense clouds phases of the Galaxy and in the outer part of the solar system that are essential to astrophysical models. These laboratory experiments allow to better constraint sputtering yields (number of constituent lost by the ice per ion), but also radiolysis and chemical composition of the sputtered material. The thickness dependence of the sputtering yield is a critical parameter, as thin ices films with respect to the probed volume may be encountered in astrophysical media. For many ices ($H_2O$, CO, $CO_2$, $O_2$ [3, 4, 5, 6, 7]) and for the stopping powers relevant to CR (Z=1 to 37, E=0.1MeV/u to 10 GeV/u) the sputtering yield for an ice of infinite thickness can be inferred. The sputtering yield is generally predicted to scale proportionally to the square of the stopping power for many low temperature molecular solid. Measurements of sputtering yields may be achieved by different methods, including microbalance, by measurements of the energy spectra of backscattered heavy projectiles (RBS) or backscattered electrons. With the advance of infrared spectrometers, and thanks to the high sputtering yield at high stopping power, direct measurements by IR absorption during the irradiation becomes accessible, and such spectrometers became routinely used in many facilities. From an experimental point of view, $N_2$ is a particular case with respect to most other ices, as it possesses a very low infrared activity (integrated band strength of $A \approx 1.3 - 1.8 \times 10^{-22}$cm/$N_2$, [8, 9], about four orders of magnitude lower than typical molecules infrared-active modes, a band located at about 2300 $cm^{-1}$). As a consequence it is difficult to employ the IR absorption method. In the literature, probably due to these experimental challenges, the sputtering yield of $N_2$ shows marked variations, and debates occurred [10] in the 90' concerning a particular behaviour of the $N_2$ ice sputtering yield as a function of the stopping power for low stopping power projectiles. A transition from a linear to quadratic evolution was hypothesised but uncertainties remains on its transition range. In this work we measured at the GANIL facility the sputtering yield for solid $N_2$ ice impacted by high stopping power projectiles. The thickness evolution was monitored during irradiation using the ice thin film Fabry-Perot interference fringes. The experiments, and the optical model used to derive ice thickness, are presented in a first section. In a second part we present the model used to reproduce the behaviour of the sputtering yield at low thickness. Finally, we present an overview of our measurements together with those from the literature and discuss about the particularity of $N_2$ ice.

## 2. Experiments

Swift ion irradiation experiments were performed at the heavy-ion accelerator Grand Accélérateur National d'Ions Lourds (GANIL). $^{58}Ni^{9+}$ projectiles were accelerated at 33 MeV on the IRRSUD beam line in May 2019. This beam was sent to an ultra high vacuum chamber, the IGLIAS (Irradiation de GLaces d'Intérêt AStrophysique) facility [11], operating in the $10^{-9}$ mbar range for the considered experiments. The $N_2$ molecular ice films were condensed on an infrared transmitting ZnSe substrate window cryocooled at 9 K. The ice films are produced by placing the cold window substrate in front of a deposition line where gaseous $^{15}N_2$ is injected. The vacuum during the experiments is dominated by infrared inactive species such as $H_2$, not sticking to the surface during the irradiation, and residual $N_2$ molecules as residual of the ice film injection sequence or from the electronic sputtering itself. We do not observe on the recorded infrared spectra any signature of $H_2O$ ice accumulation, showing that its partial pressure is much lower. In one experiment, a very small pollution of $CO_2$, with a negligible column density with respect to the ice film one, is observed in the infrared, converted to CO during the beam irradiation, and disappear during the course of the irradiation. At the ion fluxes used of $10^9$ ion/cm$^{-2}/s$, the

potential redeposition is not a strong concern on the presented results, and would contribute to slightly increase the estimated sputtering yield is the analysis presented hereafter.Two ice films were irradiated, with initial thickness of 0.3 and 1 micron, respectively. At such thicknesses, the ion beam passes through the film with an almost constant energy deposition.

At the ion energy used here, the stopping power is dominated by the electronic regime. SRIM calculations yield a value of Se $\approx 1697 \times 10^{-15}$eV cm$^2$/$^{15}N_2$ molecule. In the following, we refer to "electronic stopping power" for brevity. A Bruker Vertex 70v FTIR spectrometer with a spectral resolution of 1 cm$^{-1}$ was used. The evolution of the infrared spectra was recorded at several fluences. The infrared transmittance spectra were recorded at 12$^o$ of incidence (a correction factor of 0.978 is therefore applied to determine the normal column densities).

## 3. Analysis

### *3.1. Optical model*

As solid $N_2$ (the same is true for $^{15}N_2$) infrared activity is very low (integrated band strength of A $\approx 1.3 - 1.8 \times 10^{-22}$cm/$N_2$, [8, 9]), we recorded the amount of nitrogen ice deposited through measurements of interference fringes that are directly related to the thickness of the thin ice film. We used thicknesses of about one micron and a third of a micron, respectively. Such thicknesses are large enough to provide measurable interference fringes and thin enough to reach the complete sputtering of the film at the end of the experiment. Fig.1 and Fig.2 upper panels show the raw transmittance spectra in the 5500-1000 cm$^{-1}$ range measured as function of ion fluence. These spectra did not exhibit new strong bands upon irradiation. The production of new infrared active species during the irradiation is dominated by the azide radical ($^{15}N_3$), observed in the thick film experiment, with a doublet around 1603 and 1598 cm$^{-1}$ (see, e.g. [12] for this isotopomer assignments). The column density of the azide radical is estimated from the [13] integrated band strength of A = $7.2 \times 10^{-20}$cm/$^{15}N_3$, representing less than about 5% of the ice film composition. A few absorption bands corresponding to low amounts of CO and $CO_2$ are observed. They originate from a slight pollution during the several hours of experiments, and are present in particular in the thick film experiment, which was the first one sequentially. An optical model was fitted to the data to extract the film thicknesses. The simulated model is calculated using the rigorous expression for the transmission of a thin absorbing film, of thickness d, on a thick transparent substrate, as presented in, e.g., [14]

$$T = \frac{16\,n\,s^2}{(n+1)^3(n+s^2) - 2(n^2-1)(n^2-s^2)\cos(\phi) + (n-1)^3(n-s^2)} \quad (1)$$

In this expression, $\phi = 4\pi nd/\lambda$. The wavelength ($\lambda$) dependent refractive index s of ZnSe, used as substrate in the experiment, is taken from [15], and is shown in the upper panel of Fig.7. A refractive index of solid $N_2$ of n=1.22 is adopted, as measured by Satorre et al.[16, 17]. A least squares fit procedure is used to fit the model to the measurements and retrieve the thickness values. Due to the lack of thermalisation of the experience hall, progressive although limited, variations on the gain of the overall signal (of less than about two percents) are observed during the measurements. This slowly varying instrumental effect is compensated for in the minimisation by applying an equivalent global gain correction to the spectra. The gain variations applied in the time response is shown in the lower panels of Fig.7. The best fitted model spectra

calculated during the minimization are shown in the lower panel of Fig.1 and Fig.2.
The column density of $^{15}N_2$ ice can be estimated from

$$N_{^{15}N_2} = N_A \times \rho \times d/M_{^{15}N_2} \quad (2)$$

where $N_A$, $\rho$, d and $M_{^{15}N_2}$ are the Avogadro number, the $^{15}N_2$ ice density, the film thickness and the molar mass of $^{15}N_2$, respectively. The $^{15}N_2$ ice density adopted is $\rho = 0.94 \times 30/28$ g/cm$^3$ (0.94 g/cm$^3$ corresponds to the $^{14}N_2$ measurement from [16, 17]). Note that ion irradiations of ice films can induce an amorphous compaction of ice structures when starting from amorphous and porous ice films, that may affect the density and thus column density estimates. Compaction, given the cross-sections for other ices at such dE/dx, occurs within fluences typical of a few $10^{11}$cm$^{-2}$. With the fluences presented in this study we are in the present experiments analysing a compact $N_2$ ice sputtering phase. The very first fluence points could be affected by a compaction phase change, but we do not observe any evidence of an abrupt change at the beginning of the irradiation that would underline a significant compaction. As shown in [16, 17], $N_2$ ice deposits do not show significant changes of refractive index nor density with temperature until sublimation under our experimental conditions. We thus expect the density to be close to the one adopted from their measurements. If another density is adopted, therefore the extracted yields must be adjusted proportionally to the inverse of the newly adopted value.

### *3.2. Sputtering model*

The column density evolution of the ice molecules submitted to ion irradiation can be described, for a semi infinite (thick) film, by

$$dN/dF = -Y_s - \sigma N \quad (3)$$

With $Y_s$ the sputtering yield and $\sigma$ the radiolysis destruction rate. The observed thickness evolution is dominated by sputtering (over radiolysis with small amounts of $^{15}N_3$ discussed above). As a result, $\sigma N << Y_s$ and the column density decreases linearly with the fluence, with a slope giving the yield of sputtered molecules per ion. As shown in Fig.6, the evolution of the column densities departs from this model for column densities below about $6 \times 10^{17}$ cm$^{-2}$ in both experiments. This change occurs because the maximum depth of sputtering by individual ions for a semi infinite ice film, hereafter called the probe depth, is then larger than the film thickness, inducing a decrease in the effective yield. Considering a direct impact model where all the molecules within a sputtering effective volume are removed from the surface [3], the evolution of the sputtering yield, as a function of ion fluence (F) can be inferred. The decay of the sputtering efficiency, when reaching thin film thicknesses lower than the probe depth of ions can be set by

$$dN/dF = -Y_s^\infty \left(1 - e^{-\frac{N}{N_D}}\right) \quad (4)$$

where $Y_s^\infty$ is the semi-infinite ice film sputtering yield, and $N_D$ is the ice column density corresponding to the sputtering probe depth by an individual incident ion. This parametrisation allows a single and simple parameter estimate of the sputtering depth. Note that for $N \gg N_D$ $dN/dF \rightarrow -Y_s^\infty$ and $\rightarrow 0$ for $N \ll N_D$. The solution to this equation comes down to

$$N(F) = N_D \times \ln\left(e^{-\frac{Y_s^\infty F}{N_D} + \ln\left(e^{\frac{N_0}{N_D}} - 1\right)} + 1\right) \quad (5)$$

where $N_0$ is the initial column density. The crater resulting from sputtering has been studied experimentally [18, 19, 20, 21, 22, 23] for different materials. Detailed calculations were often conducted using molecular dynamic simulations [24, 25, 26].

In [3], craters formed by ion impact were phenomenologically described with an oversimplified cylinder shape (i.e a cross-section approach). In this work, we simulate the sputtering with a simple model generating ions with a random impact position in the x-y perpendicular to the beam propagation, irradiating a slab of solid $N_2$ molecules. Each ion sputters a volume of matter, producing a 'crater'. The model follows the evolution of the column density, as would be measured by infrared spectroscopy. We adopted two 'crater' shapes: a cylinder and a Gaussian shape (shown in Fig. 3). The former was first adopted as it allows defining easily an aspect ratio, which is the ratio of the sputtered volume typical dimensions. One dimension is taken along the ion propagation axis, the sputtering depth d, i.e. the height of the cylinder, and the other is the diameter of the cylinder (2 times its radius $r_c$), leading to an aspect ratio, $AR = d/2r_c$. The Gaussian profile is probably a better approximation for the shape of a crater. The 2D Gaussian amplitude is set to the same depth d. As both profiles are parametrised with a common and fixed depth d, they must be normalised to maintain the same sputtering volume for comparison. To maintain the same sputtered volume, the corresponding Gaussian width, defined by the standard deviation $\sigma$ is related to the cylinder radius by $\sigma = r_c/\sqrt{2}$. We generated several sets of models, each one repeated with ten independent runs. All models have in common, an approximately 2000 nm×2000 nm slab, an initial thickness scaled to an equivalent column density of $N_0 = 2\times10^{18}$ cm$^{-2}$ (corresponding to one of the experiments performed), and a sputtering depth fixed to $N_D = 4\times10^{17}$ cm$^{-2}$, that is close to the observed change in column density with the fluence for both experiments. The sets differ in the explored crater's aspect ratios, varied from one to forty. Changing the aspect ratio and keeping fixed the sputtering depth changes and defines the semi infinite sputtering yield. The simulated parameters that varies are shown in the left column of Table 1. A zoom at different irradiation times are shown in Fig.4 for one of the 2D Gaussian models. The column density evolution comparison for the Gaussian and cylinder crater shapes is presented in Fig.5. The crater shape influences differently the evolution at low column densities. Once the column density evolution with fluence was simulated with the model, it

Table 1: Model simulations fitting summary

| Model[a] | | Cylinder[b] | | | Gaussian[b] | | |
|---|---|---|---|---|---|---|---|
| Aspect Ratio | $Y^\infty$ | $N_0$ $\times10^{18}$cm$^{-2}$ | $N_D$ $\times10^{17}$cm$^{-2}$ | $Y^\infty$ | $N_0$ $\times10^{18}$cm$^{-2}$ | $N_D$ $\times10^{17}$cm$^{-2}$ | $Y^\infty$ |
| 1 | $1.41\times10^8$ | 2.00±0.02 | 6.71±0.14 | $1.56\pm0.18\times10^8$ | 2.00±0.04 | 4.07±0.62 | $1.47\pm0.07\times10^8$ |
| 3 | $1.57\times10^7$ | 2.01±0.01 | 7.12±0.12 | $1.79\pm0.07\times10^7$ | 2.00±0.01 | 4.12±0.27 | $1.62\pm0.03\times10^7$ |
| 5 | $5.65\times10^6$ | 2.01±0.01 | 6.93±0.42 | $6.40\pm0.02\times10^6$ | 2.00±0.01 | 4.09±0.23 | $5.87\pm0.08\times10^6$ |
| 10 | $1.41\times10^6$ | 2.01±0.01 | 6.87±0.31 | $1.60\pm0.03\times10^6$ | 2.00±0.01 | 4.09±0.20 | $1.47\pm0.02\times10^6$ |
| 40 | $8.83\times10^5$ | 2.00±0.01 | 6.98±0.33 | $1.02\pm0.04\times10^6$ | 2.00±0.01 | 4.00±0.16 | $9.17\pm0.01\times10^5$ |

[a] The initial column density is set to $N_D = 2\times10^{18}$ cm$^{-2}$, and the sputtering depth is fixed to $N_D = 4\times10^{17}$ cm$^{-2}$. error bars are 2 sigma standard deviations from the model fitting. [b] Fitted parameters.

was fitted with equation 5. The fitted parameters retrieved for the different fiducial models are

given in Table 1. These simulations show that the initial column density is retrieved efficiently for all models. The semi-infinite sputtering yields are reasonably well inferred in both models, with a slight overestimation in the cylinder model. A greater difference appears for the retrieved sputtering depth $N_D$. The cylinder shape approximation overestimates $N_D$ by up to 75%. This can be expected when looking at Fig.5 showing simulations of the column density evolution for two models with the same parameters, differing only in the crater shape. The model with a cylinder shape crater deviates from the semi-infinite slope behaviour earlier than the Gaussian crater shape one. The Gaussian crater shape model, as seen in Table 1 fitted parameters, allows a better fitting procedure to infer the depth within about 10%. Equation 5 thus describes adequately the 2D Gaussian sputtering crater shape.

### *3.3. Sputtering yield and depth for $N_2$*

We fitted equation 5 to the measured column density as function of projectile fluence in order to determine both the sputtering yield and the sputtering depth of the irradiated $N_2$ ice films. The column density evolution and the model fits based on equation 5 are shown in Fig.6, overlaid to the data as thick dashed red lines. The thin dashed red lines correspond to the expected evolution considering a sputtering yield independent of the thickness (i.e. kept with the semi infinite value). The result of the fit gives access to $Y_s^\infty = 8.0 \pm 1.2 \times 10^4$ sputtered $N_2$/ion, and a depth of sputtering of $N_D = 3.9 \pm 1.8 \times 10^{17}$ cm$^{-2}$, corresponding to about $5.25 \times 10^2$ monolayers assuming the ice density given above. It is difficult to constrain the sputtering contribution mediated via the interface with the ZnSe substrate. However, for completeness, we calculated the expected sputtering yield from the ZnSe substrate from literature data to evaluate its potential influence. SRIM calculations yield, for the present study Ni ions, a stopping power value in the substrate of Se $\approx 3800 \times 10^{-15}$eV cm$^2$/ZnSe. Pannu et al. [27] estimated the sputtering of ZnSe exposed to 100 MeV Ag ions to be of 300±30 Zn/ion. The stopping power of theses Ag ions is about 1.87 times higher than the Ni ions used in our study. Assuming a quadratic dependence of the yield with the stopping power, we estimate a ZnSe sputtering yield of ~86 Zn/ion, i.e. almost three orders of magnitude lower than the above measured $Y_s^\infty = 8.0 \pm 1.2 \times 10^4$ sputtered $N_2$/ion. The expected diameter of the sputtering crater for ZnSe is therefore much smaller. Given this huge difference in sputtering efficiencies, we are most probably dominated in our measurements by the $N_2$ ice behaviour. Our measurement is reported together with measurements at lower stopping power from the literature [10, 28, 29, 30] in Fig.8. A summary of these literature values and the present work is given in Table 2. When reported as a function of the electronic stopping power, this sputtering yield is in better agreement with the quadratic behaviour extrapolation from the data of [30], [29] and [28]. Data from [10] alone appears significantly below the other sets of data. The data are fitted with a power law to describe the sputtering yield as a function of the stopping power. Considering this work and the literature data above, the yield can be described by

$$Y_s^\infty = 1.69^{+7.54}_{-1.38} \times 10^{-2} \times Se^{2.04 \pm 0.40} \quad (6)$$

with Se in units of $10^{-15}$ eV cm$^2$/molecule, reported in Fig.8. This new measurement further confirms that the solid $N_2$ yield has a quadratic dependence with stopping power, a dependence holding at the large dE/dx reported in this study The evolution of $N_2$ is close to the CO sputtering yields and has a similar stopping power dependence. If $N_2$ is mixed with CO in the dense phases of interstellar molecular clouds, its sputtering should therefore proceed with a similar overall efficiency.

## 4. Conclusion

The column density evolution of low temperature solid $N_2$ films irradiated with swift heavy ions was determined with a new approach measuring the film interference fringes in the infrared spectra, and supported by an optical modelling. A model simulating the swift ions sputtered ice volume with a cylinder or a two dimensional Gaussian is proposed. The amplitude of the cylinder or Gaussian represents the sputtered species maximum depth origin induced by individual ions. We showed that the transition from a semi inifinite medium to thin film yield behaviour can adequately be described by setting an exponential decay of the sputtering yield, governed by the Gaussian sputtering depth amplitude.

We applied the model to swift ion irradiation experiments of solid $N_2$. The sputtering yield dependence on the stopping power is evaluated in light of the measured high stopping power yield. The results obtained confirm that the sputtering yield evolve quadratically with the stopping power in solid $N_2$. The discrepancy between sputtering yields previously measured at low stopping power is thus reduced, renewing the interest for additional $N_2$ ice measurements at low stopping power. Our model also determined the sputtering depth, showing that the sputtering crater left over by single ions possesses a large depth to radius aspect ratio for solid $N_2$. It would be worth investigating the general behaviour of the crater topology with Se further with explicit 3D thermal spike models, especially for the molecular solids case such as ices.


## Acknowledgements

This work was supported by the the Programme National "Physique et Chimie du Milieu Interstellaire" (PCMI) of CNRS/INSU with INC/INP co-funded by CEA and CNES, ANR COMETOR project, grant ANR-18-CE31-0011 and ANR IGLIAS project, grant ANR-13-BS05-0004, of the French Agence Nationale de la Recherche. The authors acknowledge the staff of CIMAP and GANIL for their invaluable support.


## References


[1] R. E. Johnson, W. L. Brown, Electronic mechanisms for sputtering of condensed-gas solids by energetic ions, Nuclear Instruments and Methods in Physics Research 198 (1) (1982) 103–118. doi:10.1016/0167-5087(82)90059-X.

[2] M. Toulemonde, W. Assmann, C. Dufour, A. Meftah, C. Trautmann, Nanometric transformation of the matter by short and intense electronic excitation: Experimental data versus inelastic thermal spike model, Nuclear Instruments and Methods in Physics Research B 277 (2012) 28–39. doi:10.1016/j.nimb.2011.12.045.

[3] E. Dartois, M. Chabot, T. Id Barkach, H. Rothard, B. Augé, A. N. Agnihotri, A. Domaracka, P. Boduch, Cosmic ray sputtering yield of interstellar $H_2O$ ice mantles. Ice mantle thickness dependence, Astronomy and Astrophysics 618 (2018) A173. arXiv:1809.09180, doi:10.1051/0004-6361/201833277.

[4] H. Rothard, A. Domaracka, P. Boduch, M. E. Palumbo, G. Strazzulla, E. F. da Silveira, E. Dartois, Modification of ices by cosmic rays and solar wind, Journal of Physics B Atomic Molecular Physics 50 (6) (2017) 062001. doi:10.1088/1361-6455/50/6/062001.

[5] E. Dartois, B. Augé, P. Boduch, R. Brunetto, M. Chabot, A. Domaracka, J. J. Ding, O. Kamalou, X. Y. Lv, H. Rothard, E. F. da Silveira, J. C. Thomas, Heavy ion irradiation of crystalline water ice. Cosmic ray amorphisation cross-section and sputtering yield, Astronomy and Astrophysics 576 (2015) A125. arXiv:1503.02609, doi:10.1051/0004-6361/201425415.

[6] C. Mejía, M. Bender, D. Severin, C. Trautmann, P. Boduch, V. Bordalo, A. Domaracka, X. Y. Lv, R. Martinez, H. Rothard, Radiolysis and sputtering of carbon dioxide ice induced by swift Ti, Ni, and Xe ions, Nuclear Instruments and Methods in Physics Research B 365 (2015) 477–481. doi:10.1016/j.nimb.2015.09.039.

[7] P. Boduch, E. Dartois, A. L. F. de Barros, E. F. da Silveira, A. Domaracka, X.-Y. Lv, M. E. Palumbo, S. Pilling, H. Rothard, E. Seperuelo Duarte, G. Strazzulla, Radiation effects in astrophysical ices, in: Journal of Physics Conference Series, Vol. 629 of Journal of Physics Conference Series, 2015, p. 012008. doi:10.1088/1742-6596/629/1/012008.

[8] S. A. Sandford, M. P. Bernstein, L. J. Allamandola, D. Goorvitch, T. C. V. S. Teixeira, The Abundances of Solid $N_2$ and Gaseous $CO_2$ in Interstellar Dense Molecular Clouds, Astrophysical Journal 548 (2) (2001) 836–851. doi:10.1086/319023.

[9] R. B. Bohn, S. A. Sandford, L. J. Allamandola, D. P. Cruikshank, Infrared Spectroscopy of Triton and Pluto Ice Analogs: The Case for Saturated Hydrocarbons, Icarus 111 (1) (1994) 151–173. doi:10.1006/icar.1994.1138.

[10] R. E. Johnson, M. Pospieszalska, W. L. Brown, Linear-to-quadratic transition in electronically stimulated sputtering of solid $N_2$ and $O_2$, Physical Review B 44 (14) (1991) 7263–7272. doi:10.1103/PhysRevB.44.7263.

[11] B. Augé, T. Been, P. Boduch, M. Chabot, E. Dartois, T. Madi, J. M. Ramillon, F. Ropars, H. Rothard, P. Voivenel, IGLIAS: A new experimental set-up for low temperature irradiation studies at large irradiation facilities, Review of Scientific Instruments 89 (7) (2018) 075105. doi:10.1063/1.5028056.

[12] C. S. Jamieson, R. I. Kaiser, Isotopic study of the formation of the azide radical ($N_3$), Chemical Physics Letters 440 (1) (2007) 98–104. doi:10.1016/j.cplett.2007.04.042.

[13] R. L. Hudson, M. H. Moore, The $N_3$ Radical as a Discriminator between Ion-irradiated And UV-photolyzed Astronomical Ices, Astrophysical Journal 568 (2) (2002) 1095–1099. doi:10.1086/339039.

[14] R. Swanepoel, Determination of the thickness and optical constants of amorphous silicon, Journal of Physics E Scientific Instruments 16 (12) (1983) 1214–1222. doi:10.1088/0022-3735/16/12/023.

[15] Optical Constants of Minerals and Other Materials from the Millimeter to the Ultraviolet, Aberdeen Proving Ground, Md. : US Army Armament, Munitions & Chemical Research, Development & Engineering Center, 1987.

[16] M. Á. Satorre, R. Luna, C. Millán, M. Domingo, C. Santonja, Density of Ices of Astrophysical Interest, Vol. 451 of Astrophysics and Space Science Library, 2018, Ch. 4, pp. 51–69. doi:10.1007/978-3-319-90020-9_4.

[17] M. Á. Satorre, M. Domingo, C. Millán, R. Luna, R. Vilaplana, C. Santonja, Density of $CH_4$, $N_2$ and $CO_2$ ices at different temperatures of deposition, Planetary Space Science 56 (13) (2008) 1748–1752. doi:10.1016/j.pss.2008.07.015.

[18] V. Kumar, R. Gupta, V. Chauhan, J. Ram, P. Singh, M. Prasad, R. Mehra, R. Kumar, High-energy 120 MeV $Au^{9+}$ ion beam-induced modifications and evaluation of craters in surface morphology of $SnO_2$ and $TiO_2$ nanocomposite thin films, Applied Nanoscience 9 (6) (2019) 1265–1280. doi:10.1007/s13204-019-01084-4.

[19] M. Karlušić, C. Ghica, R. F. Negrea, Z. Siketić, M. Jakšić, M. Schleberger, S. Fazinić, On the threshold for ion track formation in $CaF_2$, New Journal of Physics 19 (2) (2017) 023023. arXiv:1606.03870, doi:10.1088/1367-2630/aa5914.

[20] F. Aumayr, S. Facsko, A. S. El-Said, C. Trautmann, M. Schleberger, Single ion induced surface nanostructures: a comparison between slow highly charged and swift heavy ions, Journal of Physics Condensed Matter 23 (39) (2011) 393001. doi:10.1088/0953-8984/23/39/393001.

[21] A. M. J. F. Carvalho, A. D. Touboul, M. Marinoni, J.-F. Carlotti, C. Guasch, M. Ramonda, H. Lebius, F. Saigne, J. Bonnet, $SiO_2$-Si under swift heavy ion irradiation: A comparison between normal and grazing incidence features, Nuclear Instruments and Methods in Physics Research B 266 (12-13) (2008) 2981–2985. doi:10.1016/j.nimb.2008.03.206.

[22] R. M. Papaléo, R. Leal, C. Trautmann, E. M. Bringa, Cratering by MeV-GeV ions as a function of angle of incidence, Nuclear Instruments and Methods in Physics Research B 206 (2003) 7–12. doi:10.1016/S0168-583X(03)00683-9.

[23] L. P. Biró, J. Gyulai, K. Havancsak, A. Y. Didyk, S. Bogen, L. Frey, Use of atomic-force microscopy and of a parallel irradiation geometry for in-depth characterization of damage produced by swift Kr ions in silicon, Physical Review B 54 (17) (1996) 11853–11856. doi:10.1103/PhysRevB.54.11853.

[24] C. Anders, E. M. Bringa, H. M. Urbassek, Ejection of Glycine Molecules Adsorbed on a Water Ice Surface by Swift-heavy Ion Irradiation, Astrophysical Journal 891 (1) (2020) 21. doi:10.3847/1538-4357/ab6efe.

[25] P. Kucharczyk, A. Füngerlings, B. Weidtmann, A. Wucher, Computer simulation of sputtering induced by swift heavy ions, Nuclear Instruments and Methods in Physics Research B 426 (2018) 5–12. doi:10.1016/j.nimb.2018.04.002.

[26] N. W. Lima, L. I. Gutierres, R. I. Gonzalez, S. Müller, R. S. Thomaz, E. M. Bringa, R. M. Papaléo, Molecular dynamics simulation of polymerlike thin films irradiated by fast ions: A comparison between FENE and Lennard-Jones potentials, Physical Review B 94 (19) (2016) 195417. doi:10.1103/PhysRevB.94.195417.

[27] C. Pannu, U. B. Singh, D. C. Agarwal, S. A. Khan, S. Ojha, R. Chandra, H. Amekura, D. Kabiraj, D. K. Avasthi, A study on the consequence of swift heavy ion irradiation of Zn-silica nanocomposite thin films: electronic sputtering, Beilstein J Nanotechnol. 5 (2014) 1691–1698. doi:10.3762/bjnano.5.179.

[28] B. Stenum, O. Ellegaard, J. Schou, H. Sørensen, R. Pedrys, Sputtering of frozen gases by molecular hydro-

gen ions, Nuclear Instruments and Methods in Physics Research B 58 (3-4) (1991) 399–403. doi:10.1016/0168-583X(91)95876-F.

[29] V. Pirronello, G. Strazzulla, G. Foti, E. Rimini, Erosion yields of 4 K N2 frozen gas by MeV helium ions, Astronomy and Astrophysics 96 (1-2) (1981) 267–270.

[30] O. Ellegaard, J. Schou, H. Sørensen, P. Børgesen, Electronic sputtering of solid nitrogen and oxygen by keV electrons, Surface Science 167 (2) (1986) 474–492. doi:10.1016/0039-6028(86)90718-1.

[31] K. M. Gibbs, W. L. Brown, R. E. Johnson, Electronic sputtering of condensed $O_2$, Physical Review B 38 (16) (1988) 11001–11007. doi:10.1103/PhysRevB.38.11001.

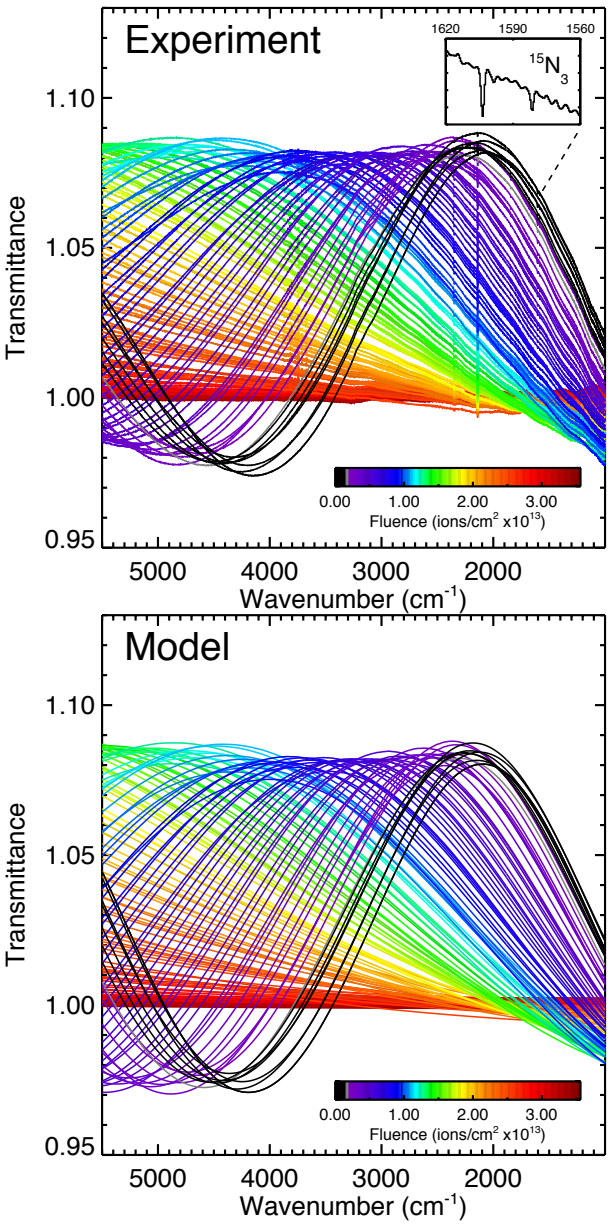


Figure 1: Upper panel: Infrared transmittance spectra of a $^{15}N_2$ ice film evolution as a function of 33MeV $^{58}Ni^{9+}$ ion fluence. The insert shows a zoom on the $^{15}N_3$ transitions arising as a doublet at 1603 and 1598 cm$^{-1}$. Lower Panel: Model spectra fitted to the data as a function of fluence. See text for model details.

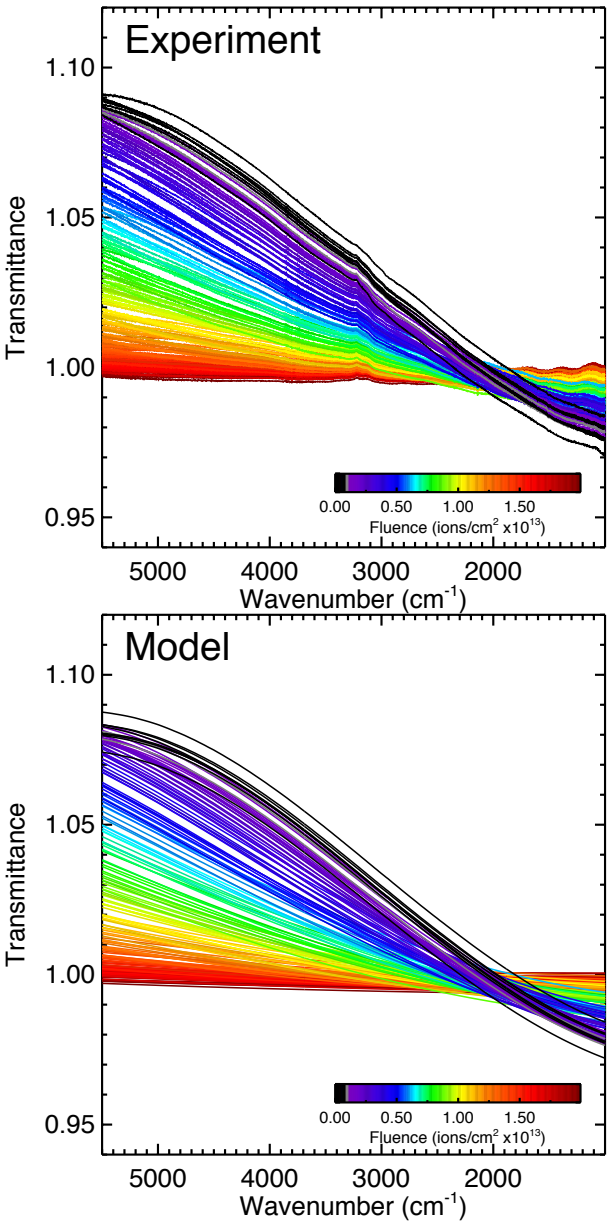


Figure 2: Upper panel: Infrared transmittance spectra of a thinner $^{15}N_2$ ice film evolution as a function of 33MeV $^{58}Ni^{9+}$ ion fluence. Lower Panel: Model spectra fitted to the data as a function of fluence. See text for model details.

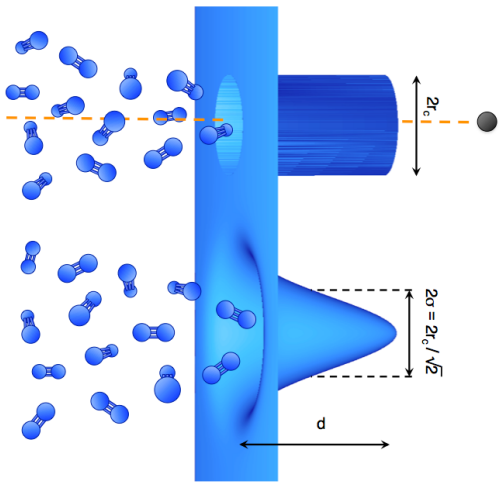


Figure 3: Schematic view of the sputtering crater models: a cylinder and 2D Gaussian. The parameters are defined with a common maximum depth d, for both shapes, and conserving the same volume.

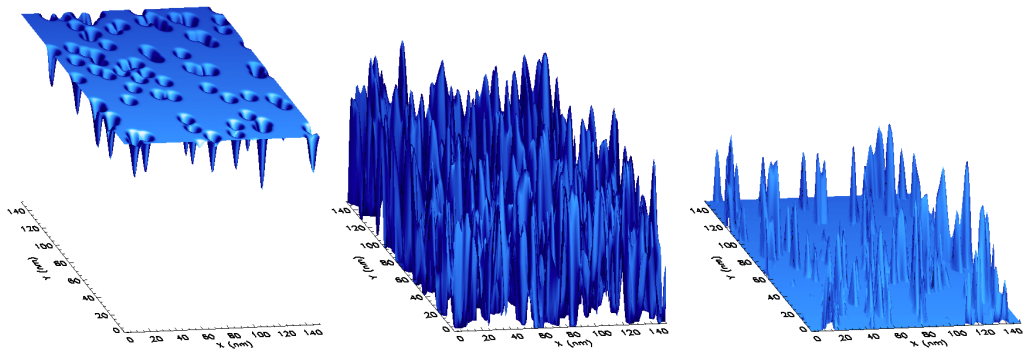

Figure 4: Snapshots of one realisation of the model with a Gaussian sputtering crater shape with an aspect ratio of 40, a depth corresponding to $N_D = 4 \times 10^{17}$ cm$^{-2}$, and an initial $N_2$ ice column density of $N_0 = 2 \times 10^{18}$ cm$^{-2}$. The left, middle, and right panels show the film topography when the column density decreased to $1.95 \times 10^{18}$ cm$^{-2}$, $5 \times 10^{17}$ cm$^{-2}$, and $2.5 \times 10^{16}$ cm$^{-2}$, respectively.

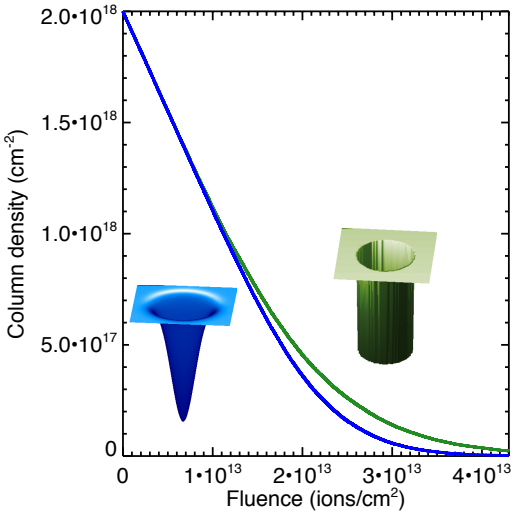


Figure 5: Comparison of 2D Gaussian (blue line, lowest curve) and cylinder (green line) crater shape on the expected column density evolution, for a model with the same sputtered volume, an aspect ratio of 40, a depth corresponding to $N_D = 4 \times 10^{17}$ cm$^{-2}$, and an initial $N_2$ ice column density of $N_0 = 2 \times 10^{18}$ cm$^{-2}$.

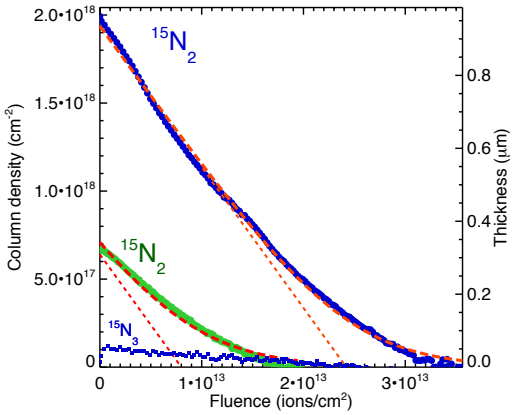


Figure 6: $^{15}N_2$ column density evolution as a function of fluence obtained from the spectra modeling fits (thick film, blue circles ;thin film, green circles). The right y-axis indicates the corresponding film thickness with the adopted density. The sputtering model for the thick film is overlaid in thick red dashed line. The expected thick film model without taking into account the finite thickness of the film is shown in thin dashed line. For the thin film, we cannot fit the model as the straight slope (semi-infinite sputtering yield) value is unconstrained. To show it behaves in the same way, the model retrieved from the thick film measurments was shifted in abscissa and overlaid. The $^{15}N_3$ column density evolution for the thick film measured via its doublet transition is shown with blue squares.

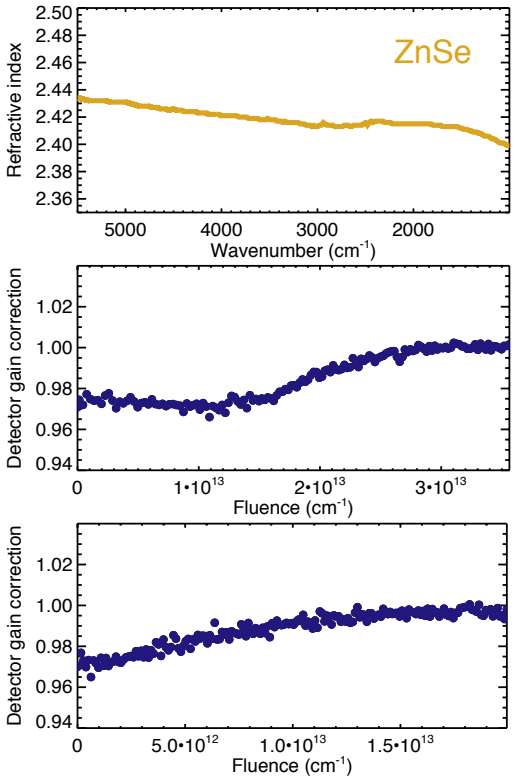


Figure 7: Upper panel: Refractive index of the ZnSe substrate used in the model calculation [15]. Middle panel: Small gain correction factor (typically $\lesssim 2\%$) applied to the spectra of the $^{15}N_2 \sim 1\mu$m thick film and used in the modeling of the fringe pattern to retrieve the film thickness. Note that we clearly see the transition from the day to night experiment hall variations. Lower panel: Small gain correction factor (typically $\lesssim 2\%$) applied to the spectra of the $^{15}N_2 \sim 0.3\mu$m thin film and used in the modeling of the fringe pattern to retrieve the film thickness.

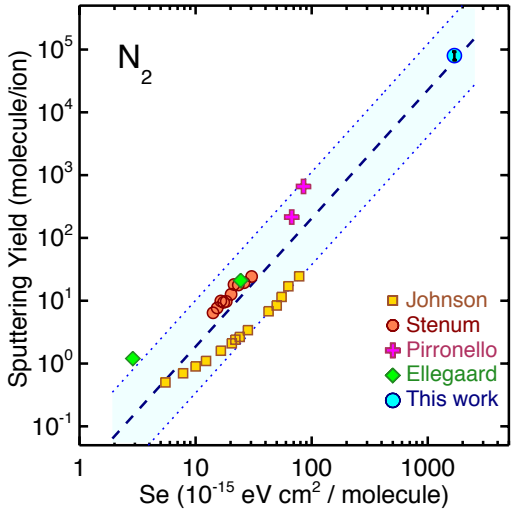


Figure 8: Solid $N_2$ sputtering yield in function of the stopping power, including measurements from the literature [10, 28, 29, 30]. The fitted evolution of the sputtering with the stopping power is shown with the blue dashed line. The error on the absolute scale of the evolution is shown with the filled light blue region.

Table 2: $N_2$ electronic sputtering experiments

| T(K) | Ion | Energy (MeV) | Se([a]) | Yield | Ref. |
|---|---|---|---|---|---|
| <10 | $H^+$ | [b] | 14.1 | 6.4 | [b] |
| <10 | $H^+$ | [b] | 15.3 | 7.7 | [b] |
| <10 | $H^+$ | [b] | 16.5 | 9.9 | [b] |
| <10 | $H^+$ | [b] | 17.5 | 9.4 | [b] |
| <10 | $H^+$ | [b] | 18.4 | 9.7 | [b] |
| <10 | $H_2^+$ | [b] | 20.2 | 12.7 | [b] |
| <10 | $H_2^+$ | [b] | 23.3 | 17.8 | [b] |
| <10 | $H_2^+$ | [b] | 26.1 | 19.4 | [b] |
| <10 | $H_3^+$ | [b] | 21.4 | 18.1 | [b] |
| <10 | $H_3^+$ | [b] | 30.4 | 24.3 | [b] |
| 10 | $H^+$ | 2.5 | 5.5 | 0.5 | [c] |
| 10 | $H^+$ | 1.5 | 7.8 | 0.7 | [c] |
| 10 | $H^+$ | 1.0 | 10 | 0.9 | [c] |
| 10 | $H^+$ | 0.8 | 12.3 | 1.1 | [c] |
| 10 | $H^+$ | 0.5 | 16.5 | 1.6 | [c] |
| 10 | $H^+$ | 0.36 | 20.5 | 2.1 | [c] |
| 10 | $H^+$ | 0.32 | 22 | 2.4 | [c] |
| 10 | $H^+$ | 0.26 | 24 | 2.65 | [c] |
| 10 | $H^+$ | 0.2 | 28.2 | 3.4 | [c] |
| 10 | $He^+$ | 1.5 | 78 | 24.5 | [c] |
| 10 | $He^+$ | 2 | 63 | 17 | [c] |
| 10 | $He^+$ | 2.5 | 55 | 11.5 | [c] |
| 10 | $He^+$ | 3 | 50 | 8.4 | [c] |
| 10 | $He^+$ | 4 | 42.5 | 6.8 | [c] |
| 10 | $He^+$ | 1 | 85.1 | 660 | [d] |
| 10 | $He^+$ | 1.8 | 67.3 | 215 | [d] |
| 10 | $He^+$ | 0.03 | 24.46 | 21 | [e] |
| 10 | $e^-$ | 0.002 | 2.88 | 1.2 | [e] |
| 10 | $^{58}Ni^{9+}$ | 33 | 1697 | $8\pm1.2\times10^4$ | |

[a] in units of $10^{-15}$ eV $cm^2/N_2$ [b] [28], beam used are in the 1.5-10 keV/u range, the yield and stopping powers are extracted from the authors Fig.1 and renormalised to be expressed per $N_2$ molecule. [c] [10, 31]; $H^+$ data with a linear dependence of the yield in function of the (lower) stopping power are not included. [d] [29] [e] [30]; the sputtering by 2 keV electrons is also shown for comparison.